Modeling and Synthesis of 3-D Water Vapor Fields for EM Wave Propagation Applications

Lorenzo Luini, *Member*, *IEEE*

***Abstract*— SMOV (Stochastic MOdel of water Vapor), a methodology to generate realistic three-dimensional spatially correlated water vapor fields is presented, which is devised by investigating remote sensing observations acquired by the MODIS sensor (Aqua satellite). Synthetic water vapor fields are 200 km×200 km, with 1 km×1 km horizontal spatial resolution, while the water vapor content *v* extends up to 20 km with a vertical sampling of 100 m. The field synthesis relies on the stochastic approach proposed by Bell and requires as input the average integrated water vapor content provided with coarse spatial and temporal resolution by NWP products. The vertical profile of *v* is modelled as a simple exponential function decreasing with height, as observed from typical RAOBS and NWP data. Tests on the model's accuracy show that both first-order (Complementary Cumulative Distribution Function - CCDF) and second-order (spatial distribution) statistics of the integrated water vapor content are closely reproduced in several European sites. Results corroborate the use of SMOV as part of a comprehensive simulator of atmospheric impairments, which aims at taking into account all the constituents affecting the propagation of millimeter-waves in different scenarios, including applications involving very low elevation links such as UAVs and LEO satellites.**

***Index Terms*— Electromagnetic wave propagation, atmospheric effects, water vapor.**

I. Introduction

THE last decade has been characterized by a large diversification and increase in millimeter-wave communication systems. On the one hand, new high-data rate interactive services, e.g. those provided via satellite to offer global Internet connectivity [1], are pushing towards the employment of higher frequency bands giving access to wider bandwidths (Ka band nowadays, Q/V bands as the next step [2]); on the other hand, new applications involving very low elevation links are being increasingly employed (e.g. Unmanned Aerial Vehicle – UAVs) or are planned to be implemented in the near future (e.g. Ka-band links from ground stations to Low Earth Orbit – LEO – satellites [3] and deep-space probes [4]).

In this context, the system design task becomes more and more critical, not only because the higher is the frequency, the larger is the detrimental impact of the atmosphere on the link (induced by hydrometeors, clouds and gases), but also because for very low elevations links (say angles smaller than 10 degrees) specific modeling needs to be properly considered, such as the Earth's curvature, the ray bending effect and the large-scale spatial distribution of the atmospheric constituents. In such scenarios, even in clear sky conditions (sole presence of gases in the atmosphere), the path attenuation might exceed several dBs (especially in tropical/equatorial sites) [5], such that taking in due account the modeling aspects mentioned above would definitely increase the accuracy of the estimated link performance. In order to meet these needs, the recent tendency in the theoretical research on millimeter-wave propagation is to move from empirical models, typically limited in their applicability to specific climatic regions, frequency ranges and/or scenarios, to highly sophisticated physically-based methodologies which inherently aim at being globally applicable and are sufficiently flexible to allow simulating with increased accuracy and reliability the impact of the atmosphere on several different millimeter-wave communication systems.

This contribution presents the development and assessment of SMOV (Stochastic MOdel of water Vapor), a methodology to synthesize statistically meaningful sets of three-dimensional (3-D) water vapor fields. SMOV represents a key element, which, together with MultiEXCELL (for precipitation) [6] and SMOC (for clouds) [7], contributes to the development of a comprehensive simulator of weather disturbances affecting the propagation of millimeter-waves [8]. SMOV reproduces the spatial distribution of the water vapor content *v* (this abbreviation − in place of the more common WVC − is used throughout this contribution in order to deal with more compact equations) with high resolution across large areas (200 km×200 km×20 km with 1 km×1 km horizontal detail and 100 m vertical sampling) starting from the generation of spatially correlated Gaussian fields, as explained in [9]. To this aim, the model relies on some key information on *v* extracted from the water vapor fields observed by the MODIS sensor onboard the Aqua satellite. Inputs to SMOV are the time series of the integrated water vapor content *V* (as for *v*, this abbreviation is preferred here to the more customary – yet less compact − IWVC), part of Numerical Weather Prediction

Manuscript received XXXX.
Lorenzo Luini is with the Dipartimento di Elettronica, Informazione e Bioingegneria, Politecnico di Milano, Piazza Leonardo da Vinci, 32, 20133, Milano, Italy, and with the Istituto di Elettronica e di Ingegneria dell'Informazione e delle Telecomunicazioni (IEIIT), Consiglio Nazionale delle Ricerche, Via Ponzio 34/5, Milano 20133, Italy (e-mail: lorenzo.luini@polimi.it).

(NWP) data provided e.g. by the European Centre for Medium-range Weather Forecast (ECMWF) over a low-resolution latitude×longitude grid (1.125°×1.125°) every 6 hours. The remainder of the paper is organized as follows: Sections II and III deals with the investigation and modeling of the horizontal and vertical distribution of water vapor, respectively, while Section IV describes in detail the procedure for the synthesis of realistic 3-D water vapor fields. Tests to evaluate the accuracy of SMOV in reproducing first- and second-order statistics of V are shown in Section V and, finally, Section VI draws some conclusions.

II. Horizontal distribution of water vapor

A. The reference water vapor dataset

The reference water vapor database used in this work originates from the MODIS sensor onboard the Aqua satellite, which flies along Low Earth Orbit (LEO) orbit covering the whole Globe with a repetition period of approximately two days. The MODIS instrument, whose main aim is to observe large-scale global dynamics of oceanic and tropospheric processes, collects radiance data in 36 optical channels (wavelengths between 0.4 and 14.4 μm) with high spatial resolution (from 250 m to 5 km footprint, linear size) implementing automatic in-flight calibration procedures [10]. Raw data are processed by the MODIS Characterization Support Team (MCST) to provide high quality calibrated products for several Earth science applications [11].

Specifically, maps of V with dimensions of 200 km×2000 km and spatial resolution of 5 km×5 km, appropriate to adequately sample the spatial distribution of water vapor, are freely available on the web for research purposes. In particular, in this work, we have employed the maps derived from 3090 swaths over Europe (20° E ≤ latitude ≤ 62° E and 10° W ≤ longitude ≤ 37° E) in 2010. As an example, Fig. 1 depicts the integrated water vapor content as observed by MODIS along a swath over Africa and Europe. Furthermore Fig. 2 depicts the Complementary Cumulative Distribution Function (CCDF) of the integrated water vapor as obtained from an extensive dataset of radiosonde observations (RAOBS) collected at Milano Linate airport between 1980 and 1989 and as extracted from MODIS data in the same area (100 km×100 km centered over the airport). The satisfactory agreement between the two curves gives a hint on the good quality of MODIS-derived water vapor data.

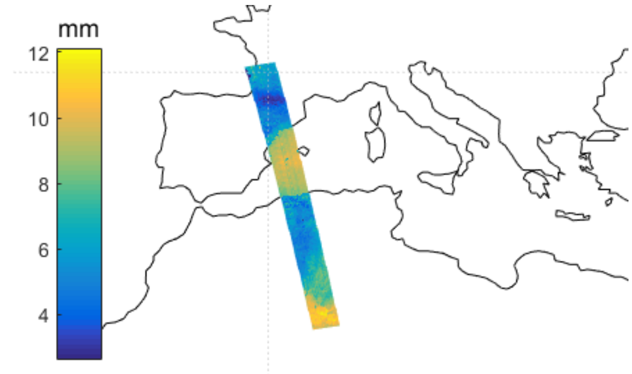

Fig. 1. Example of the spatial distribution of integrated water vapor V, as observed by MODIS on a swath over Africa and Europe.

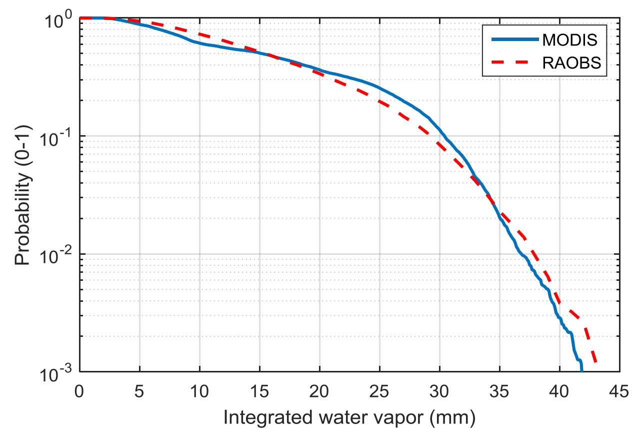

Fig. 2. CCDF of the integrated water vapor as obtained from an extensive dataset of radiosonde observations collected at Milano Linate airport between 1980 and 1989 (red dashed line) and as extracted from MODIS data in the same area (100 km×100 km centered over the airport).

B. Characterization of water vapor horizontal distribution

As a first step to investigate the key properties of water vapor fields, we have partitioned the large swaths into 200 km×200 km maps to achieve dimensions typical of Numerical Weather Prediction (NWP) products such as 2°×2° latitude/longitude.

The analysis of the horizontal distribution of the integrated water vapor content within each 200 km×200 km map showed that the values of V tend to follow the Weibull distribution:

$$p(V) = \frac{B_w}{A_w}\left(\frac{V}{A_w}\right)^{B_w-1} \exp\left[-\left(\frac{V}{A_w}\right)^{B_w}\right] \tag{1}$$

where A_W and B_W are the scale and shape parameters, respectively, regulating the expression in (1). This finding confirms what is discussed in [12] and is clearly exemplified in Fig. 3, where a sample water vapor field observed by MODIS (top) and the associated statistical characterization of V (bottom) is provided in terms of Cumulative Distribution Function (CDF). The bottom figure title reports E_V, the value of V averaged over the whole area, as well as A_W and B_W of the Weibull distribution fitting data with good accuracy (maximum likelihood estimation - MLE). This is quantified by E_ε and RMS_ε in the figure legend, i.e. the average and root mean square values, respectively, of the error figure ε defined

This is the author's version of an article that has been published in this journal. Changes were made to this version by the publisher prior to publication.
The final version of record is available at http://dx.doi.org/10.1109/TAP.2016.2591062

as:

$$\varepsilon(P) = 100\frac{V_f(P) - V_m(P)}{V_m(P)} \tag{2}$$

In (2), $V_m(P)$ and $V_f(P)$ are the V values (mm) associated to the reference (MODIS) and MLE CDFs, respectively, at probability levels P ranging from 0 to 1 with step of 0.001.

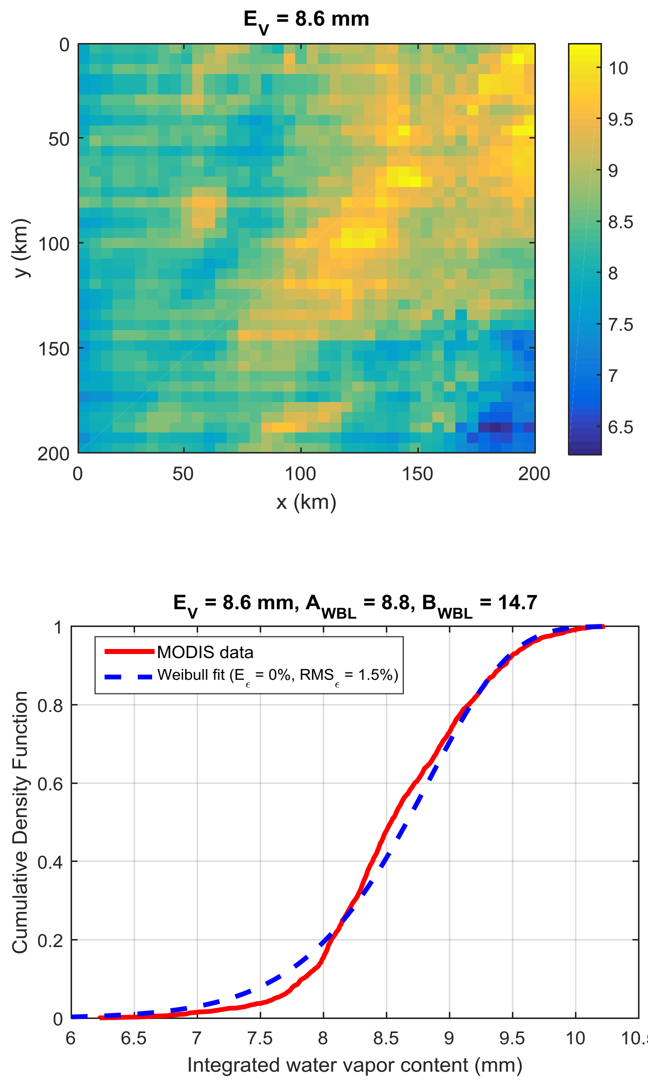

Fig. 3. Sample MODIS water vapor field (top) and statistical characterization of V (bottom).

Considering the whole MODIS dataset, Fig. 4 depicts the trend of the average E_ε (solid line with triangles) and RMS_ε (dashed line with stars) as a function of E_V, together with the percentage number of MODIS maps falling in each E_V class (blue bars). As it turns out, E_V is distributed according to the Weibull distribution, and, in addition, results confirm that in each map V tends to closely follow the same distribution, being the fitting slightly more accurate for larger values of E_V.

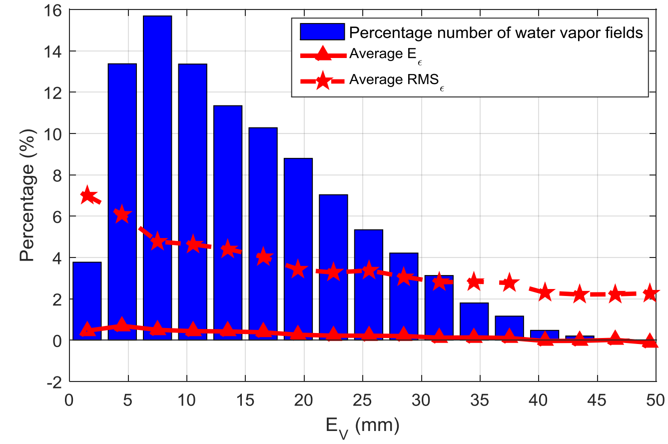

Fig. 4. Trend of the average E_ε (solid line with triangles) and RMS_ε (dashed line with stars) as a function of the average integrated water vapor content E_V, together with the percentage number of MODIS fields considered in each E_V class (blue bars).

All the MODIS-derived 200 km×200 km maps were afterwards processed to identify possible relationships of E_V with A_W and B_W. As for the former, A_W was found to be proportional to E_V, with the very high linear correlation shown in Fig. 5 (see the inset in the figure for more details):

$$A_W = 1.044 E_V \tag{3}$$

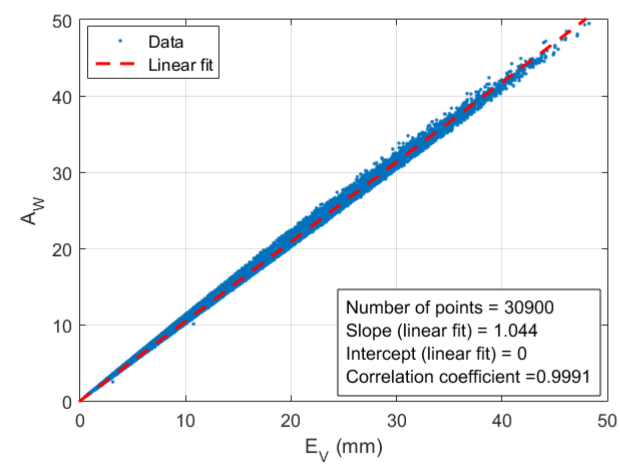

Fig. 5. Relationship between A_W and E_V.

Concerning the second parameter of the Weibull distribution, as shown in Fig. 6, the scatterplot between E_V and B_W turned out to be rather spread, which prevents from defining a simple analytical expression relating the two quantities. On the other hand, the conditional lognormal probability density function $p(B_W|E_V)$ in (4) was found to be well suited for modeling the statistical relationship between B_W and E_V:

$$p(B_W \mid E_V) = \frac{1}{B_W\,\sigma(E_V)\sqrt{2\pi}}\exp\left[-\frac{\left(\ln B_W - \mu(E_V)\right)^2}{2\sigma(E_V)^2}\right] \tag{4}$$

where μ and σ, which are both function of E_V, are the mean and standard deviation values of the natural logarithm of B_W, respectively. A hint of the modeling accuracy of (4) is given by Fig. 7, which depicts $p(B_W|E_V)$ for two classes of E_V (low values on the top and high values on the bottom), including μ and σ of the fitting MLE lognormal distribution.

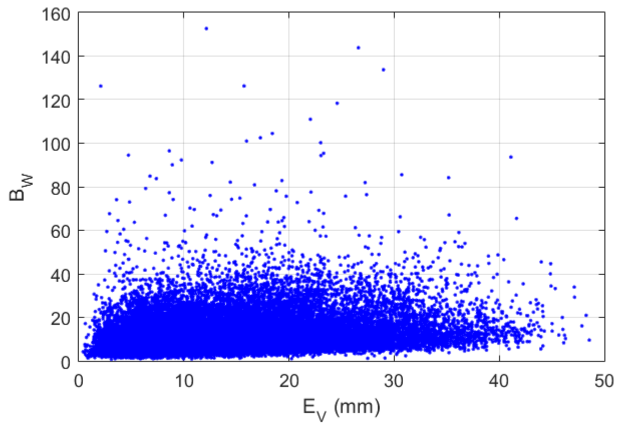

Fig. 6. Scatterplot between B_W and E_V.

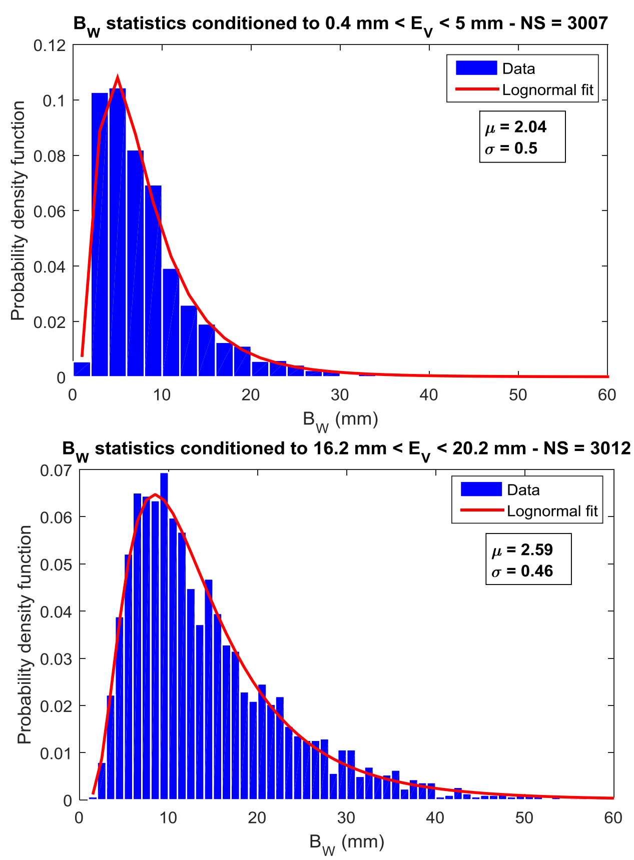

Fig. 7. Examples of $p(B_W|E_V)$, the statistical distribution of B_W conditioned to E_V; low and high values of E_V on the top and bottom side, respectively. Empirical data and MLE lognormal distributions.

For the complete characterization of $p(B_W|E_V)$, we have defined eight E_V bins of different width but containing roughly the same number of samples ($NS \approx 3000$). The maximum error in fitting the empirical $p(B_W|E_V)$ with the MLE lognormal distributions (specifically, root mean square values of the percentage relative difference error) is 8%. In addition, as can be inferred from Fig. 8 and Fig. 9, both μ and σ show quite a regular trend with E_V (blue squares indicate the center values of each class), which can be closely approximated by the following analytical expressions:

$$\begin{aligned}\mu(E_V) &= -1.408\,E_V^{0.239} + 6.885\,E_V^{0.097} - 3.725\\ \sigma(E_V) &= -2.228\,E_V^{0.156} + 6.66\,E_V^{0.06} - 3.962\end{aligned} \tag{5}$$

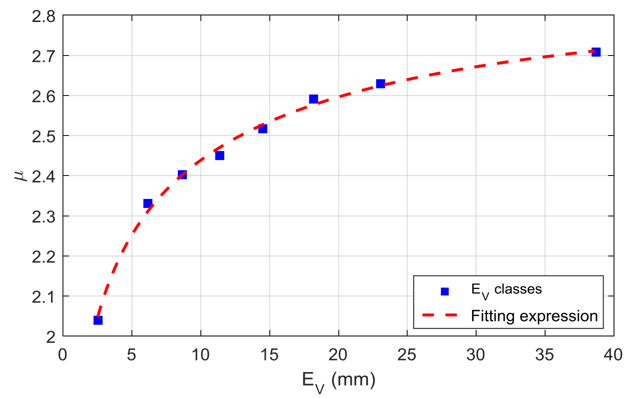

Fig. 8. Trend of μ with E_V.

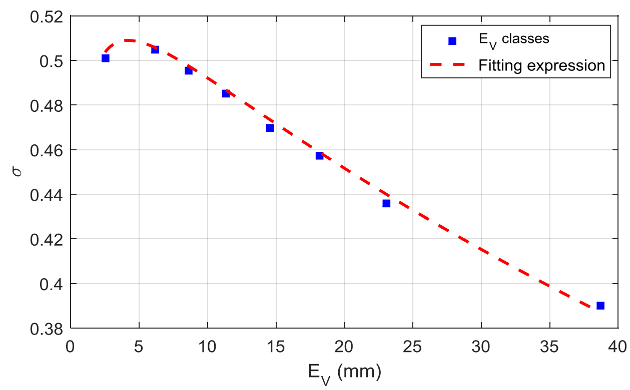

Fig. 9. Trend σ with E_V.

The additional information needed to generate synthetic water vapor fields concerns the spatial variability of V, which was studied by resorting to the correlation index ρ [13]:

$$\rho(\mathbf{x},\mathbf{y}) = \frac{\mathrm{E}[V(\mathbf{x})\cdot V(\mathbf{y})] - \mathrm{E}[V(\mathbf{x})]E[V(\mathbf{y})]}{\sigma[V(\mathbf{x})]\,\sigma[V(\mathbf{y})]} \tag{6}$$

E[•] and σ[•] in (6) indicate the mean and standard deviation, whereas $V(\mathbf{x})$ and $V(\mathbf{y})$ represent the integrated water vapor content time series, respectively associated to pixels $\mathbf{x}$ and $\mathbf{y}$ in each 200 km×200 km water vapor map. An underlying assumption in the calculation of ρ is the spatial stationarity of the water vapor (also valid for precipitation [13]); this entails that the spatial correlation between two points depends (mostly) on their distance and only marginally on their position, i.e.:

This is the author's version of an article that has been published in this journal. Changes were made to this version by the publisher prior to publication.
The final version of record is available at http://dx.doi.org/10.1109/TAP.2016.2591062

$$\rho(\mathbf{x},\mathbf{y}) = \rho(d = |\mathbf{x}-\mathbf{y}|) \tag{7}$$

Fig. 10 shows the spatial correlation of V calculated by averaging ρ values associated to pairs of pixels at the same distance d (red line): besides showing that the water vapor decorrelates slowly with distance, the limited spread of ρ around its average value (density scatter plot, higher concentration in darker areas) definitely validates the spatial stationarity assumption mentioned above.

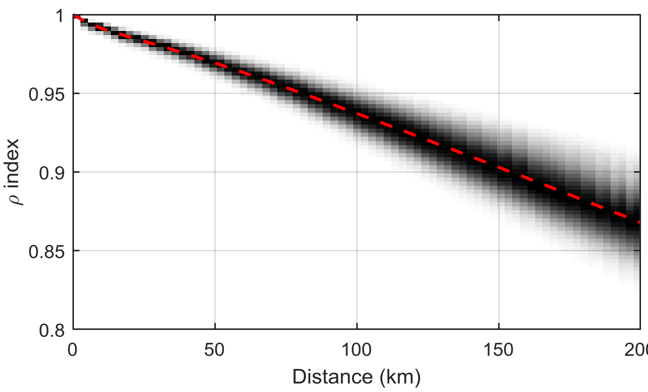

Fig. 10. Decorrelation with distance of the integrated water vapor content calculated from MODIS data (red dashed line). Also depicted is the spread of ρ around its average value (gray scale density scatter plot, higher concentration in darker areas).

In order to synthesize realistic water vapor fields according to [9], random Gaussian fields with spatial correlation $\rho_G(d)$, to be known a priori, need to be first generated. The mean $\rho_G(d)$ can be estimated by first converting each MODIS water vapor field into a Gaussian field, which, under the assumption of Weibull distribution for V, corresponds to employing (14) and (15) reported in Section III below. Afterwards the spatial correlation of the random Gaussian process was evaluated from converted maps using the same definition of ρ as in (6) and assuming again spatial stationarity. The resulting average $\rho_G(d)$ is well fitted by the following analytical expression:

$$\rho_G(d) = 1.656 e^{-\frac{d}{232.56}} - 0.337 e^{-\frac{d}{71.43}} - 0.319 \tag{8}$$

where d is expressed in km.

III. Vertical Development of Water Vapor

As can be inferred from RAOBS and NWP data [14], the vertical profile of water vapor density v follows a fairly regular trend, which is typically modeled using the following exponential profile:

$$v(h) = v_G\, e^{-h/h_V} \tag{9}$$

In (9), v_G is the water vapor content at sea level (g/m^3) and h_V is the exponential decay rate, also known as water vapor scale height. An example of a typical vertical profile of the water vapor density is shown in Fig. 11: the black curve comes from the data measured by the radiosonde launched in Milano Linate airport, Italy, while the red line is obtained from fitting (9) to such data (in this case v_G = 2.6 g/m^3 and h_V = 1.48 km).

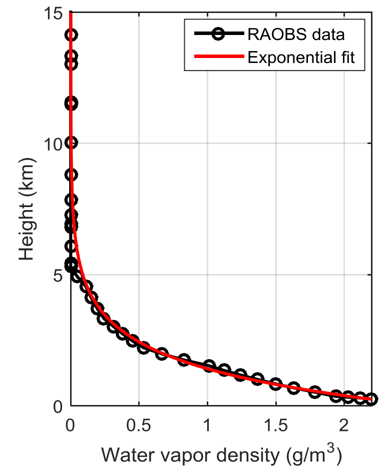

Fig. 11. Typical profile of the water vapor density v with height (data from the radiosonde launched at Milano Linate airport, Italy) and associated exponential fit in (9), with v_G = 2.6 g/m^3 and h_V = 1.48 km.

Based on (9), if the integrated water vapor content V and the water vapor scale height h_V are known, v_G can be derived by imposing:

$$V = \int_{0\text{ km}}^{20\text{ km}} v_G\, e^{-h/h_V}\, dh \tag{10}$$

which, inverted after simple passages, leads to:

$$v_G = \frac{V}{h_V}\left(1 - \mathrm{e}^{-\frac{20\text{ km}}{h_V}}\right) \approx \frac{V}{h_V} \tag{11}$$

The integral in (10) is calculated up to 20 km, which is approximately the upper limit of the troposphere; the approximation on the right hand side of (11) is justified by common values of h_V, which are typically comprised roughly between 0.5 km and 4 km.

As a result, starting from a V field generated by SMOV and knowing h_V, the full three-dimensional distribution of the water vapor content v is given by:

$$v(x,y,h) = \frac{V(x,y)}{h_V} e^{-h/h_V} \tag{12}$$

IV. Full Procedure for Water Vapor Field Synthesis

On the basis of the analysis reported in previous sections, the horizontal synthesis of V over the target area can be obtained starting from $\rho_G(d)$ in (8), and from E_V and h_V. As for E_V, this information can be derived from NWP products, such as the ECMWF (European Centre for Medium-range Weather Forecast) ERA-40 dataset: in this work, we have taken advantage of the area-averaged integrated water vapor content

V_{ERA} sampled every 6 hours and characterized by spatial resolution of 2°×2° (latitude×longitude), i.e. roughly 200 km×200 km in Europe. As for h_V, time series are not directly available in the ERA-40 database, but statistics and monthly average values are included in recommendation ITU-R P.836-5 [15]. Based on these inputs, the procedure involves the following steps:

1. Given the site of interest with coordinates (lat,lon), extract from the ERA-40 database times series of the average integrated water vapor content (V_{ERA}) and derive from recommendation ITU-R P.836-5 monthly mean values of the water vapor scale height ($h_{V,m}$) associated to values relative to the four surrounding grid pixels.
2. Scale the V_{ERA} values, each of which is associated to the reference height h_{ERA} of the ERA-40 pixel (ground), to derive the integrated water vapor content at the sea level $V_{ERA,sea}$. As recommended by ITU-R in P.836-5, this is achieved again by considering that the integrated water vapor decays exponentially with height, i.e.:

$$V_{ERA,sea} = V_{ERA}\exp\left(-\frac{h_{sea}-h_{ERA}}{h_{V,m}}\right) = V_{ERA}\exp\left(\frac{h_{ERA}}{h_{V,m}}\right) \quad (13)$$

3. As recommended in P.836-5, bilinearly interpolate the values of $V_{ERA,sea}$ and $h_{V,m}$ on the site of interest with coordinates (lat,lon), thus obtaining $V'_{ERA,sea}$ and $h'_{V,m}$. Finally $E_V = V'_{ERA,sea}$ and $h_V = h'_{V,m}$.
4. Using E_V, calculate μ and σ as from the expressions in (5), which define $p(B_W|E_V)$ in (4).
5. Calculate A_W from E_V using the linear relationship in (3).
6. ~~Randomly extract~~Obtain B_W as a random draw from the lognormal distribution $p(B_W|E_V)$ derived at step 4.
7. Generate a random Gaussian field $g(x,y)$ (zero mean and unit variance) with the spatial correlation ρ_G in (8) according to [9].
8. Convert the Gaussian field $g(x,y)$ into a water vapor field (Weibull distribution) $V(x,y)$ according to:

$$U(x,y) = \frac{1}{2}\left[1 + erf\left(\frac{g(x,y)}{\sqrt{2}}\right)\right] \quad (14)$$

$$V(x,y) = A_W\left[-\ln\left(1-U(x,y)\right)\right]^{\frac{1}{B_W}} \quad (15)$$

Equation (14) turns the Gaussian field into a random field with values uniformly distributed between 0 and 1 (U), while equation (15) converts the uniform field into the target water vapor field characterized by the Weibull distribution with parameters A_W and B_W (erf is the error function).

9. Derive the full spatial distribution of the water vapor density v using (12), which extends vertically from the sea level up to 20 km.
10. Truncate the v field according to the height of the site of interest h_{stat} by discarding v values for which $h < h_{stat}$.

Fig. 12 shows a sample field (V in mm) reflecting the input values extracted from the ERA-40 database (E_V = 18.9 mm), while Fig. 13 depicts the spatial distribution of v calculated by means of (12) starting from the synthetic field shown in Fig. 12; the bottom graph reports v on the y/h plane for x = 120 km, while the top graph shows the associated integrated water vapor content V as a function of y.

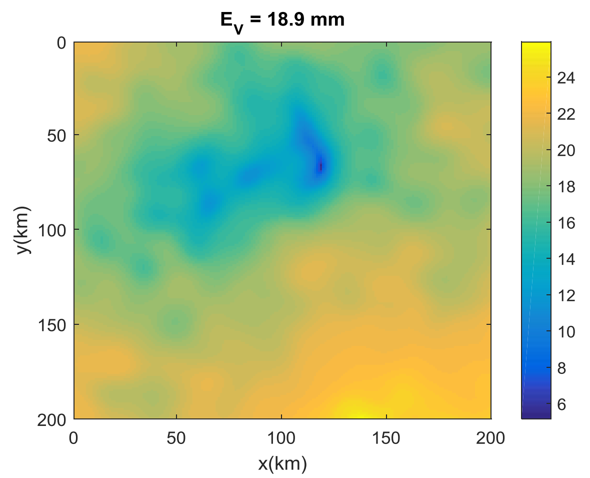

Fig. 12. Sample water vapor field generated by SMOV starting from ERA-40 data with 2°×2° spatial resolution and 6-hour temporal resolution.

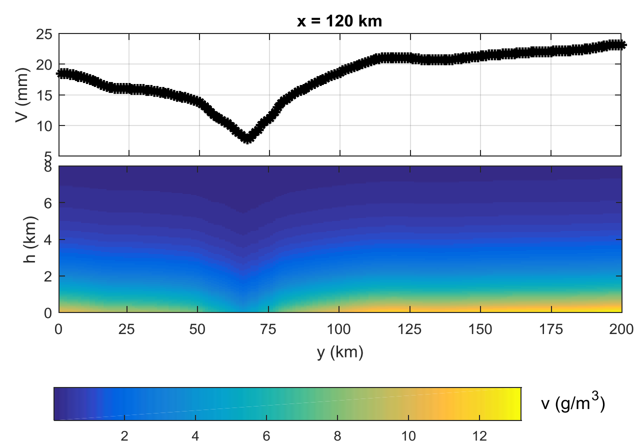

Fig. 13. Spatial distribution of v calculated by means of (12) starting from the field of V shown in Fig. 12. Bottom graph: v on the y/h plane for x = 120 km; top graph: associated integrated water vapor content V as a function of y.

V. Validation of SMOV

A. Accuracy in reproducing realistic water vapor fields

In order to test SMOV, using as input the ERA-40 time series of V_{ERA} in the period 1996-2000, we have calculated first- and second-order statistics of V starting from 7308 synthetic water vapor fields (200 km×200 km×20 km with 1 km×1 km horizontal detail and 100 m vertical sampling)~~(time~~

This is the author's version of an article that has been published in this journal. Changes were made to this version by the publisher prior to publication.
The final version of record is available at http://dx.doi.org/10.1109/TAP.2016.2591062

~~series of V_{ERA} in the period 1996-2000)~~. The reference statistics of V used to assess the performance of SMOV were derived for 14 European sites where extensive RAOBS data were collected (and whose accuracy was duly checked) for 10 years (1980-1989): specifically the sites span very different climatic regions, from Sodankyla in Finland to Trapani in Southern Italy [16].

As an example, Fig. 14 compares the CCDF of V estimated from SMOV with the one obtained from the RAOBS data collected in De Bilt, The Netherlands.

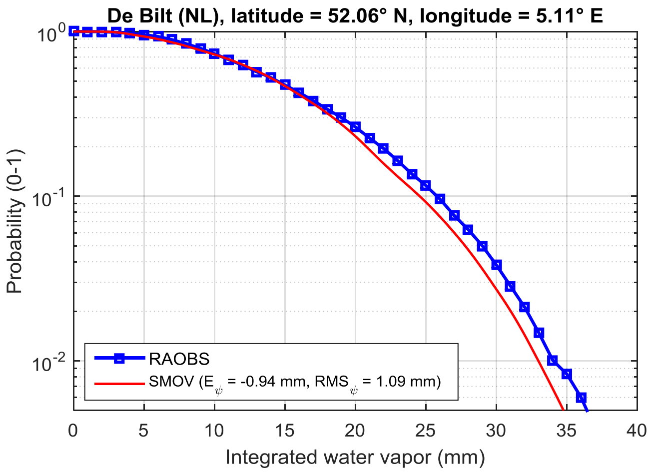

Fig. 14. Validation of SMOV against RAOBS data collected in De Bilt, The Netherlands (1980-1989). Input values to SMOV are V_{ERA} values extracted from the ERA-40 database in the period 1996-2000.

The good agreement between the two curves in Fig. 14 is quantified in the figure legend, which includes the average (E_ψ) and root mean square (RMS_ψ) values of the error ψ ($P \geq 5\times10^{-3}$), defined as:

$$\psi(P) = V_E(P) - V_R(P) \tag{16}$$

In (16), $V_E(P)$ and $V_R(P)$ are the predicted and reference integrated water vapor contents, respectively, associated to the same probability level P.

Fig. 15 extends the prediction accuracy assessment to the whole set of 14 sites (as in Fig. 14, for the calculation of E_ψ and RMS_ψ, P ranges between 5×10^{-3} and 1). Results in Fig. 15 show that SMOV achieves an overall very good accuracy in modeling first-order statistics of V.

The ability of SMOV in reproducing the spatial distribution of V was evaluated against the average decorrelation trend (ρ as defined in (6)) extracted from MODIS data. Fig. 16 compares this curve (large black dashed line) with all the ones associated to the synthetic water vapor fields generated by SMOV for the above 14 European sites (thin lines). The discrepancies in ρ from site to site (at 150 km the correlation index varies from 0.85 to 0.95, i.e. approximately 10%) reflect the different climate which the 14 locations are subject to (typically drier in the North and more humid in the South). Overall, the agreement between the average decorrelation trend obtained from SMOV (dashed red line) and the MODIS curve is very good (the root mean square value of the relative difference between the two curves is 0.7%).

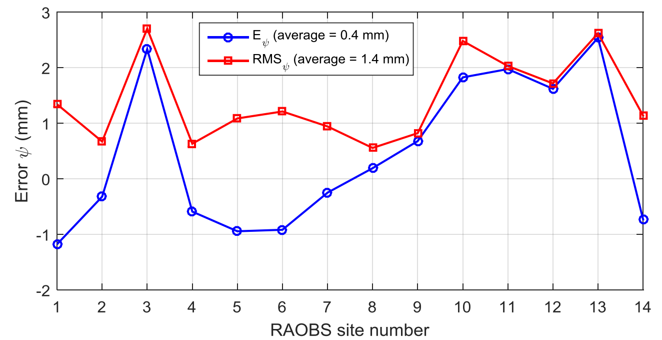

Fig. 15. Validation of SMOV against all RAOBS data available: first-order statistics. Input values to SMOV are V_{ERA} values extracted from the ERA-40 database (1996-2000).

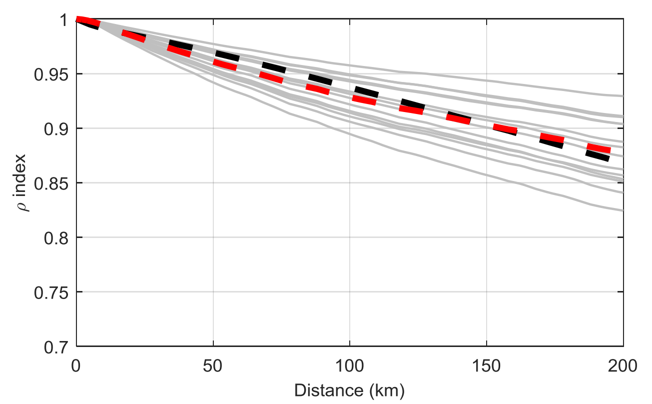

Fig. 16. Validation of SMOV against MODIS data: second-order statistics. Input values to SMOV are V_{ERA} values extracted from the ERA-40 database (1996-2000).

VI. Attenuation Induced by Water Vapor on Earth-Space Links

This section presents some examples of the use of SMOV to estimate the attenuation induced by water vapor (A_V) on Earth-space links.

Fig. 17 shows the CCDF of A_V calculated for a hypothetical Earth-space link between an Earth Observation (EO) satellite flying along a near-polar Low Earth Orbit (LEO) and a ground station, set in Svalbard Islands, Norway (latitude 78.75° N, longitude 16° E, 10 m a.m.s.l.), from which the satellite is often visible. The elevation angle is $\theta = 10°$, assumed here as a possible minimum elevation for which the satellite is tracked, and the link frequency is 26 GHz, a band allocated for data downlink in future EO missions. The path attenuation is calculated by first integrating v along the link to obtain the slant integrated water vapor content V_S, and afterwards by employing the methodology presented in [17], according to which A_V can be calculated from the simple knowledge of V_S by exploiting the concept of mass absorption coefficient (specifically, refer to equation (7) in [17]). It is worth pointing out that, in order to improve the prediction accuracy and by taking advantage of the full 3-D spatial distribution of v, in calculating A_V, the Earth's curvature has been taken into account (calculation according to section 2.2 of recommendation ITU-R P.676-10 [18]), as well as the ray bending effect associated to the standard atmospheric profile for which the gradient of the refractive index with height close to the ground, dn/dh, is assumed to be -40×10^{-6} km^{-1} [19]. Depicted in the same picture are the CCDFs of the attenuation due to rain (A_R) and clouds (A_C) as calculated according to ITU-R recommendation (e.g. P.840-6 for the latter [20]). For the selected site, results indicate that the contribution of water vapor is dominant for outage probabilities P higher than 3%, and that A_V is anyway larger than A_R for $P \geq 0.5\%$.

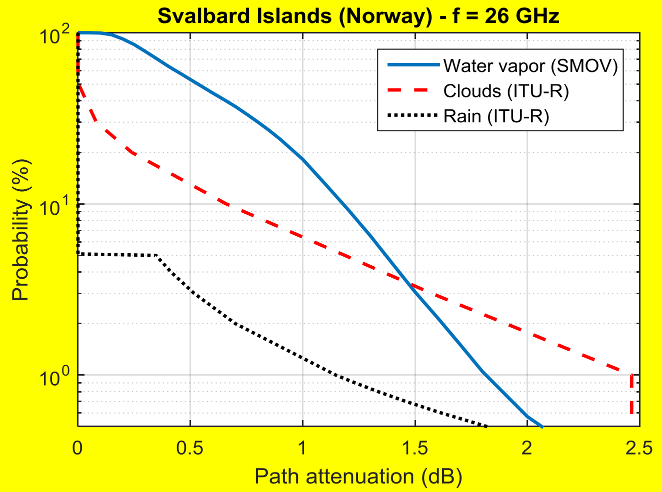

Fig. 17. Prediction of the attenuation due to water vapor (using SMOV), clouds and rain (using ITU-R recommendations) for a site in the Svalbard Islands, Norway (latitude 78.75° N, longitude 16° E, 10 m a.m.s.l.). Frequency 26 GHz, 10° elevation angle.

Contrary to the example reported in Fig. 17, in which tropospheric attenuation turns out to be quite limited due to the extremely cold climate affecting Svalbard Islands, Fig. 18 reports much higher levels of attenuation due to water vapor, rain and clouds.

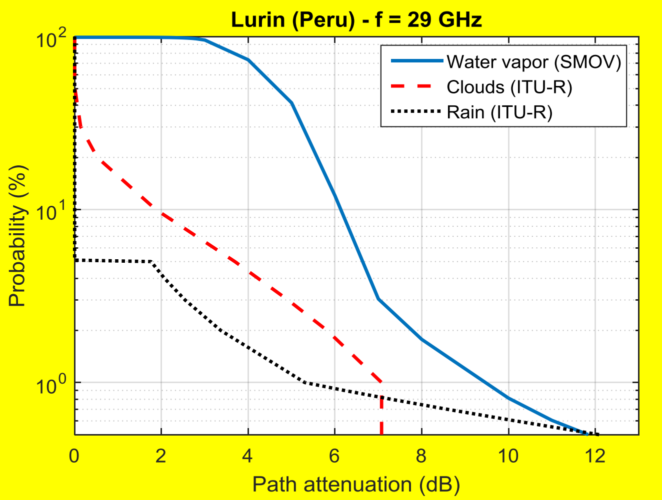

Fig. 18. Prediction of the attenuation due to water vapor (using SMOV), clouds and rain (using ITU-R recommendations) for Lurin, Peru (latitude -12.2° N, longitude 76.9° W, 9 m a.m.s.l.). Frequency 29 GHz, 10° elevation angle.

This second example refers to Lurin, Peru (latitude -12.2° N, longitude 76.9° W, 9 m a.m.s.l.), where an O3b gateway operates to upload contents to the 12 Medium Earth Orbit (MEO) telecommunications satellite of the company [21]. The frequency of the link is 29 GHz, used by O3b for the uplink, and the elevation angle is again 10°. The gateway site is characterized by a rather dry climate (according to recommendation ITU-R P.837-6, the probability to have rain is 1.5% and the rain rate exceeded for 0.01% of the time is approximately 14 mm/h) and by fairly limited cloud coverage (according to recommendation ITU-R P.840-6, the probability to have clouds is roughly 50%), whereas, as clearly visible in Fig. 18, the impact of water vapor is definitely significant due to the tropical climate affecting the site: the water vapor attenuation exceeded for 0.5% of the time is around 12 dB, in the same order of A_R.

As a final example, Fig. 19 reports the attenuation statistics for a link operating at 50 GHz between the geostationary satellite KA-SAT (orbital position 9° E) with the EUTELSAT gateway installed in a site close to Turin, Italy (latitude 45.1° N, longitude 7.6° E, 290 m a.m.s.l.). In this case the elevation angle is fixed to 38.1° and A_V has a much more limited contribution to the total attenuation.

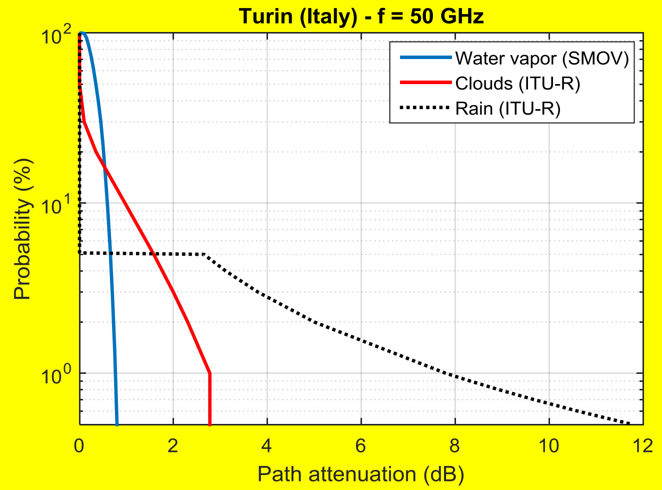

Fig. 19. Prediction of the attenuation due to water vapor (using SMOV), clouds and rain (using ITU-R recommendations) for Turin, Italy (latitude 45.1° N, longitude 7.6° E, 290 m a.m.s.l.). Frequency 50 GHz, 38.1° elevation angle.

VII. CONCLUSIONS

This contribution presents SMOV (Stochastic Model Of water Vapor), a method for the synthesis of three-dimensional spatially correlated water vapor fields (200 km×200 km×20 km with 1 km×1 km horizontal detail and 100 m vertical sampling) from Numerical Weather Prediction (NWP) products (reanalysis or forecasts) with coarse spatial (e.g. 1.125°×1.125° latitude×longitude grid) and temporal resolution (6 hours). Fields of integrated water vapor content V are generated by taking advantage of the stochastic approach developed by Bell and SMOV main parameters were determined from high-resolution MODIS-derived water vapor fields. The data investigation pointed out that V values in each map tend to follow the Weibull distribution, whose parameters turn out to depend on E_V, the V value averaged over the target area. As expected the spatial correlation of V was found to decrease very slowly with distance (at 200 km distance, the spatial correlation index ρ is roughly 0.87). Moreover, the vertical development of the water vapor content v is modeled as a simple exponential function decreasing with height, as typically observed from RAOBS and NWP data.

The model's accuracy was tested against radiosonde data collected in 14 sites ranging from Northern (Sodankyla, Finland) to Southern (Trapani, Italy) Europe using as input to SMOV five years of E_V time series extracted from the ERA-40 database: predicted CCDFs of V closely reproduce the ones estimated from RAOBS data (overall, for all sites, the root mean square of the error on the CCDF of V equal to 1.4 mm). Moreover, the average spatial correlation characterizing synthetic V fields is in very good accordance with the one derived from the MODIS database. Finally, SMOV has been applied to estimate the impact of water vapor attenuation in three sites affected by different climates (cold, tropical and temperate). ~~These~~ All the results shown in this contribution corroborate the use of SMOV as part of a comprehensive simulator of atmospheric impairments, which aims at taking into account all the constituents affecting the propagation of millimeter-waves in different scenarios, including applications involving very low elevation links such as UAVs and LEO satellites.

Acknowledgment

This effort was sponsored by the Air Force Office of Scientific Research, Air Force Material Command, USAF, under grant number FA8655-13-1-3081. The U.S Government is authorized to reproduce and distribute reprints for Governmental purpose notwithstanding any copyright notation thereon. The authors would also like to acknowledge: the MODIS scientists and associated NASA personnel for the production of the data used in this work; the ECMWF for granting access to the water vapor dataset included in the ERA-40 database; Dr. Martellucci from the European Space Agency for the provision of radiosonde data.

References

[1] http://space.skyrocket.de/doc_sdat/directv-10.htm, Accessed March. 2016.

[2] A. Kyrgiazos, B. Evans, P. Thompson, N. Jeannin, "Gateway diversity scheme for a future broadband satellite system," Advanced Satellite Multimedia Systems Conference and 12th Signal Processing for Space Communications, pp. 363 – 370, 2012.

[3] "Channel modelling for design of Earth observation 26 GHz data downlink systems", ESA ESTEC Study No. 4000105326/12/NL/LvH, 2015.

[4] "Assessment of propagation effects in the W bands for space exploration," ESA ESTEC Study No. 21317/07/NL/HE, 2011.

[5] P. Bouchard, "Approximate Method for Estimating Gaseous Loss at Very Low Angles Along Paths of Finite Length and Earth-Space Paths," *IEEE Transactions on Antennas and Propagation*, 64 (2), 687-699.

[6] L. Luini, C. Capsoni, "MultiEXCELL: a new rain field model for propagation applications," *IEEE Transactions on Antennas and Propagation*, vol. 59, no. 11, Page(s): 4286 – 4300, November 2011.

[7] L. Luini, C. Capsoni, "Modeling High Resolution 3-D Cloud Fields for Earth-space Communication Systems," *IEEE Transactions on Antennas and Propagation*, vol. 62 (10) , pp. 5190 - 5199, 2014.

[8] L. Luini, C. Capsoni, "Joint Effects of Clouds and Rain on Ka-Band Earth Observation Data Downlink Systems", *EuCAP 2015*, pp. 1-5, 12-17 April 2015, Lisbon, Portugal.

[9] T. L. Bell, "A Space-Time Stochastic Model of Rainfall for Satellite Remote-Sensing Studies," *Journal of Geophysical Research*, Vol. 92, No. D8, pp. 9631-9643, 1987.

[10] X. Xiong, W. Barnes, "An Overview of MODIS Radiometric Calibration and Characterization," *Adv. Atmos. Sci.*, vol. 23, issue 1, pp. 69-79, 2006.

[11] Members of the MODIS Characterization Support Team, "MODIS Level 1B Product User's Guide," July 20, 2012, available online at http://mcst.gsfc.nasa.gov/sites/mcst.gsfc/files/file_attachments/M1054D_PUG_083112_final.pdf.

[12] N. Jeannin, L. Feral, H. Sauvageot, L. Castanet, "Statistical Distribution of Integrated Liquid Water and Water Vapor Content From Meteorological Reanalysis," *IEEE Transaction on Antennas and Propagation*, Volume: 56, Issue: 10, Page(s): 3350-3355, 2008.

[13] L. Luini, C. Capsoni, "On the Relationship Between the Spatial Correlation of Point Rain Rate and of Rain Attenuation on Earth-Space Radio Links," *IEEE Transactions on Antennas and Propagation*, vol. 61, no. 10, Page(s): 5255 - 5263, October 2013.

[14] L. Luini, C. Capsoni, "Using NWP Reanalysis Data for Radiometric Calibration in Electromagnetic Wave Propagation Experiments," *IEEE Transactions on Antennas and Propagation*, vol. 64, no. 2, Page(s): 700 - 707, February 2015.

[15] Water vapour: surface density and total columnar content. Geneva, 2013, ITU-R recommendation P. 836-5.

[16] COST Action 255 Final Report, "Precipitation, Clouds and Other Related Non-Refractive Effects," J. P. V. Poiares Baptista, Ed. Noordwijk, The Netherlands: ESA Publication Division, ch. 3.2.

[17] L. Luini, C. Riva, "Improving the Accuracy in Predicting Water Vapor Attenuation at Millimeter-wave for Earth-space Applications", *IEEE Transactions on Antennas and Propagation*, vol. 64, no. 6, Page(s): XX - XX, June 2016.

[18] ITU-R Recommendation P.676-10, Attenuation by atmospheric gases. Geneva, Switzerland, 2013.

[19] ITU-R Recommendation P.452-16, Prediction procedure for the evaluation of interference between stations on the surface of the Earth at frequencies above about 0.1 GHz. Geneva, Switzerland, 2015.

[20] ITU-R Recommendation P.840-6, Attenuation due to clouds and fog. Geneva, Switzerland, 2013.

[21] http://www.o3bnetworks.com/. Accessed June 2016.